Nanocomposite desalination membranes made of aromatic polyamide with cellulose nanofibers: synthesis, performance, and water diffusion study

Complete List of Authors:	Cruz-Silva, Rodolfo; Shinshu University Faculty of Engineering, Research Initiative for Supra-Materials; Shinshu University Faculty of Engineering, COI Aqua Innovation Center Izu, Kazuo; Shinshu University Faculty of Engineering, COI Aqua Innovation Center Maeda, Jun; Shinshu University Faculty of Engineering, COI Aqua Innovation Center Saito, Shigeru; Shinshu University Faculty of Engineering, COI Aqua Innovation Center Morelos-Gomez, Aaron; Shinshu University Faculty of Engineering, Faculty of Engineering Aguilar, Celia; Shinshu University Faculty of Engineering, COI Aqua Innovation Center; Universidad Autonoma de Nuevo Leon, Facultad de Ingenieria Mecanica y Electrica Takizawa, Yoshihiro; Shinshu University Faculty of Engineering, COI Aqua Innovation Center Yamanaka, Ayaka; Research Organisation for Information Science and Technology Tokyo Tejima, Syogo; Research Organisation for Information Science and Technology Tokyo Fujisawa, Kazunori; Shinshu University Faculty of Engineering, Research Initiative for Supra-Materials; Shinshu University Faculty of Engineering, COI Aqua Innovation Center Takeuchi, Kenji; Shinshu University Faculty of Engineering, Research Initiative for Supra-Materials; Shinshu University Faculty of Engineering, COI Aqua Innovation Center Hayashi, Takuya; Shinshu University Faculty of Engineering, Research Initiative for Supra-Materials; Shinshu University Faculty of Engineering, COI Aqua Innovation Center Noguchi, Toru; Shinshu University Faculty of Engineering, Resarch Initiative for Supra-Materials; Shinshu University Faculty of Engineering, COI Aqua Innovation Center Isogai, Akira; The University of Tokyo, Graduate School of Agricultural and Life Sciences Endo, Morinobu; Shinshu University Faculty of Engineering

SCHOLARONE™
Manuscripts

ARTICLE

Nanocomposite desalination membranes made of aromatic polyamide with cellulose nanofibers: synthesis, performance, and water diffusion study.

Rodolfo Cruz-Silva,[a,b] Kazuo Izu,[b] Jun Maeda,[b] Shigeru Saito,[b] Aaron Morelos-Gomez,[a,b] Celia Aguilar,[b,c] Yoshihiro Takizawa,[b,†] Ayaka Yamanaka,[d] Syogo Tejiima,[d] Kazunori Fujisawa,[a,b] Kenji Takeuchi,[a,b] Takuya Hayashi,[a,b] Toru Noguchi,[a,b] Akira Isogai,[e] and Morinobu Endo.[a,b]

Reverse osmosis membranes of aromatic polyamide (PA) reinforced with a crystalline cellulose nanofiber (CNF) were synthesized and their desalination performance were studied. Comparison with plain PA membranes shows that the addition of CNF reduced the matrix mobility resulting in a molecularly stiffer membrane because of the attractive forces between the surface of the CNFs and the PA matrix. Fourier transform-infrared spectroscopy and X-ray photoelectron spectroscopy results showed complex formation between the carboxy groups of the CNF surface and the *m*-phenylediamine monomer in the CNF-PA composite. Molecular dynamics simulations showed that the CNF-PA had higher hydrophilicity which was key for the higher water permeability of the synthesized nanocomposite membrane. The CNF-PA reverse osmosis nanocomposite membranes also showed enhanced antifouling performance and improved chlorine resistance. Therefore, CNF shows great potential as a nanoreinforcing material towards the preparation of nanocomposite aromatic PA membranes with longer operation lifetime due to its antifouling and chlorine resistance properties.

Introduction

Reverse osmosis (RO) membrane desalination has experienced dramatic growth in the last 30 years.[1] This has been accomplished by a combination of factors that include population and economic growth in developing countries,[2] water scarcity due to climate change[3] and tighter environmental regulations that have been enforced in recent years.[4] The first commercially successful desalination membranes were discovered in the early 60s by Loeb and Soubaranian.[5] These membranes were made by phase inversion, based on cellulose acetate, and they are still used due to their robustness, and particularly due to their excellent chlorine resistance. However, currently the most cost-effective membranes for seawater desalination are those based on crosslinked aromatic polyamide (PA).[1] These membranes were

discovered in the late 70s by Cadotte.[6] While many improvements have been done on its surface modification,[7] its bulk chemical structure remains largely unmodified for most commercial applications. Fortunately, in the last 10 years, researched have been done in the modification of these membranes with nanomaterials such as silica nanoparticles,[8, 9] zeolites,[10,11] carbon nanotubes.[12-27] Nanocomposite aromatic PA membranes usually improve its chlorine resistance,[18,23, 28] water permeation rate,[14,20] and antifouling performance[24, 26, 27] although these improvements often come with a trade-off in salt rejection. Recently, due to the better understanding of the mechanism of diffusion of these types of membranes,[29] important improvements in salt rejection have been achieved. Among the recently developed nanomaterials, cellulose nanofibers (CNFs) have attracted great attention due to their interesting properties and environmentally friendly features.[30] They are water dispersible at nanometer levels, presumably almost non-toxic,[31] chemically resistant, and yet biodegradable. Saito and Isogai reported CNF preparation by the TEMPO mediated oxidation route that allowed the production in large-scale under environmentally friendly conditions.[32]

Nanocellulose can be used to reinforce polymers, improving their mechanical properties, particularly increasing the Young's modulus without increasing the composite weight.[33] However, there are scarce reports on the use of CNFs[34,35] and cellulose nanocrystals (CNCs)[36-46] in nanocomposite membranes using crosslinked aromatic PA as the matrix. The use of CNF combined with PA to prepare RO membranes is completely different to the use of cellulose in cellulose acetate membranes, which has been used for a long time to make RO membranes.

a. Research Initiative for Supra-Materials, Faculty of Engineering, Shinshu University 4-17-1 Wakasato, Nagano-city 380-8553, Japan.
b. Aqua Innovation Center, Faculty of Engineering, Shinshu University 4-17-1 Wakasato, Nagano-city 380-8553, Japan.
c. Facultad de Ingenieria Mecánica y Electrica, FIME, Universidad Autonoma de Nuevo Leon, Ave. Pedro de Alba s/n, Ciudad Universitaria, C.P. 66455, San Nicolas de los Garza, N.L., Mexico.
d. Research Organization for Information Science & Technology, Sumitomo-Hamamatsucho Building, 1-18-16, Hamamatsucho, Minato-ku, Tokyo, 105-0013, Japan.
e. Department of Biomaterial Sciences, Graduate School of Agricultural and Life Sciences, The University of Tokyo, Bunkyo-ku, Tokyo 113-8657, Japan.
† Present Address: National Institute of Technology, Nagano College; 716 Tokuma, Nagano 381-0041, Japan.
Electronic Supplementary Information (ESI) available: [details of any supplementary information available should be included here]. See DOI: 10.1039/x0xx00000x

Here, we show that CNFs can improve not only water permeation rate and chlorine resistance but also reduce fouling. The use of a sustainable polymer such as cellulose and the improvements in the membrane service-life have a high potential due to the requirements for green desalination and environmentally friendly technologies. We have combined theoretical studies based on molecular dynamics and first principles with experimental results to understand the potential of CNF for advanced reverse osmosis membranes, the mechanism of water diffusion, and ion rejection and its beneficial effect on chlorine resistance.

Results and discussion

Synthesis and characterization.

Cellulose nanocrystals and CNFs can be obtained from different cellulose sources using different methods, which affects the physicochemical characteristics of composite membrances,[47] Thus, we first characterized the CNF material used in this study. The AFM image (Figure S1a) of CNF showed elongated fibrils of 3-4 nm in diameter and several hundreds of nanometers in length. The wide-angle X-ray scattering (WAXS) pattern and its radial integration are shown in Figure S1b and Figure S1c, respectively. The typical 200 peak was shown at 16 Å-1, suggesting mainly the cellulose I type polymorph. The XPS wide scan in Figure S1d shows the C, O, N and Na 1s peaks. The sodium originates from the surface of the TEMPO-oxidized CNFs present as the counterion of carboxylate groups.[48] The presence of carboxyl groups were also confirmed by the deconvolution of the C 1s core-level spectrum (Figure S1e) and the FT-IR spectra of the CNF film (Figure S1f).

The structure model of the CNF is depicted in the diagram in Figure S2. TEMPO-oxidized CNF was provided as its water dispersion. We thus used the aqueous phase for the CNF-PA membrane synthesis. After the synthesis, the membranes were analyzed by AFM, SEM, and TEM and the images are shown in Figure 1. A characteristic ridge and valley morphology, which is typical of aromatic PAs[49] were observed in the AFM height and SEM images of the plain PA (Figure 1a and Figure 1b, respectively). The TEM image in Figure 1c showed a cross-section of the membrane where the porous polysulfone and the selective PA layer were seen. This image showed typical PA lobes that rose well above (ca. 400 nm) the polysulfone surface. The addition of CNF to aromatic PA resulted in a slight change in the morphology (Figure 1d). The surface roughness of the samples was assessed by measuring the root mean square (RMS) from the AFM height images and showed that the RMS decreased from 68 nm to 41 nm upon addition of CNF into PA. The SEM image of the CNF-PA sample (Figure 1e) showed more incomplete ridge formation, compared to the ring-like shape of the ridges in the plain PA surface. The TEM cross-sectional image (Figure 1f) was consistent with a surface with lower roughness, compared to the PA membrane.

The selective layers were transferred to a silicon wafer by dissolving the support membrane and observed in both sides from SEM and TEM images. Figure S3a shows the morphology of the CNF-PA membrane, which showed mechanical properties good enough to manipulate it even after removing the polysulfone support membrane. The selective layer was scratched to reveal the back of the selective layer (Figure S3b). Detailed observation of the surface and backside of the CNF-PA membrane (Figure S3c and S3d, respectively) showed a striking difference in the morphology. While on the surface apparently no CNFs material was seen, the backside of the membrane revealed a fibrous material that might correspond to a morphology induced by CNF.

XPS analysis of the surface of the plain PA membrane with both the wide scan and C1s core level peak (Figure S4a and Figure S4b) showed a similar composition to the corresponding CNF-PA membrane spectra (Figure S4c and Figure S4d). This result indicates that most of the CNF remained embedded at the bottom part of the RO membrane, because the C 1s peak of the CNF membrane usually showed a large presence of C-O groups (Figure S1e). A similar composition was confirmed by semiquantitative XPS analysis and by deconvoluting the components of the C1s spectra (Table S1), which showed that CNF addition did not affect the surface chemical composition of the membranes.

Both PA and CNF-PA membranes removed from thin-film nanocomposite membranes were analyzed by TEM (Figure S5a and S5b, respectively) and STEM (Figure S5c and S5d). Unfortunately, TEM could not detect clearly the CNF component from the PA matrix, because the electron densities of CNF and PA are quite similar. STEM relies on atomic number, and both PA and CNF contain C and O elements. Nevertheless, features such as thickness/roughness were translated to changes in contrast that showed a more homogeneously thick and consequently less surface-rough CNF-PA membrane.

With this information, we propose a model for the membrane formation. During the interfacial polymerization, the monomer MPD molecule, which has both a higher affinity to the organic phase and a higher molecular diffusion to the hydrophilic CNF. Consequently, the top layer consisted basically of aromatic PA, while the bottom of the membrane was rich in CNF. These asymmetric membranes with a gradient composition might combine the separation ability of the top layer with the mechanical properties of the bottom layer without having an interfacial stress plane. Figure S6 shows the membrane models for both PA (Figure S6a) and CNF-PA (Figure S6b). These models are consistent with the similar experimental values of salt rejection rates from both membranes. Indeed, only a slight improvement from 99.5% rejection rate for the plain PA membrane, to 99.6% for the CNF-PA membrane was achieved. It is well known that most of the ion rejection phenomena occurs in the surface and top section of the active layer, and since both membranes have almost the same surface chemical composition as shown in Figure S4, similar salt rejection rates are expected. On the other hand, water permeability, did show a clear increment from 0.59 m^3/day·m^2 for the plain PA membrane to 0.81 m^3/day·m^2 for the CNF-PA membrane. Water permeability is related to the water diffusion across the membrane, and thus we carried out molecular dynamics
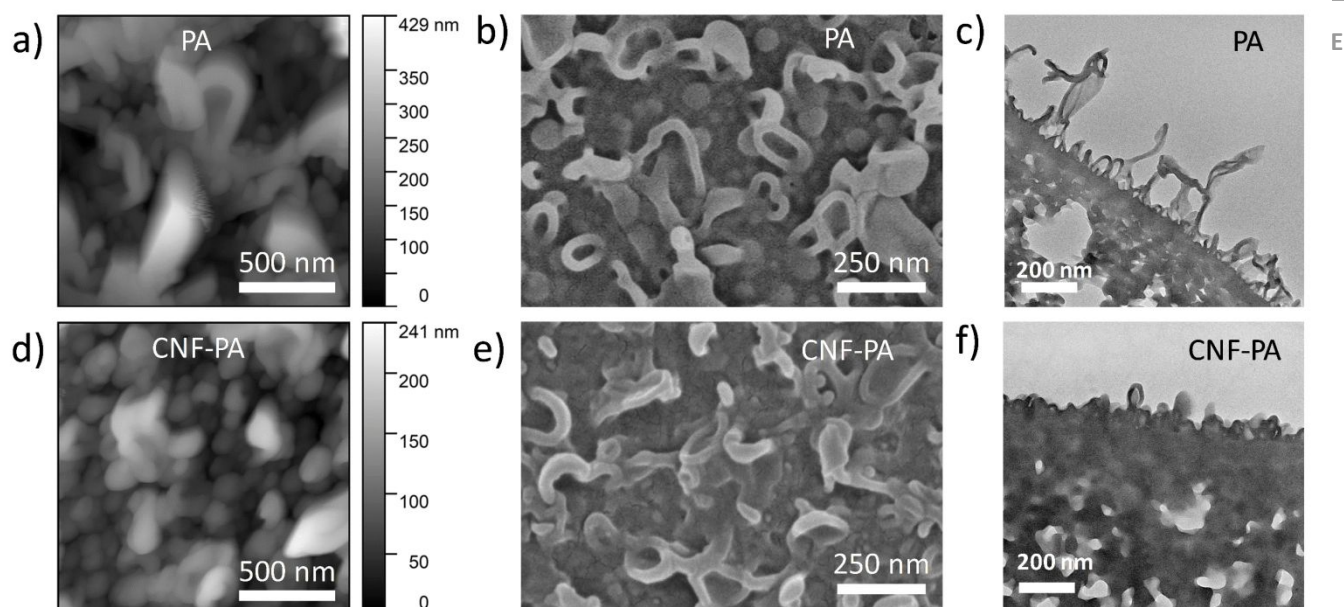
Figure 1. Morphology of the membranes synthesized. a) AFM height mode, b) SEM, and c) TEM cross-section image of the of plain PA membrane. d) AFM height mode, e) SEM, and f) cross-section TEM images of a CNF-PA membrane.

simulations to understand the difference in the water transport mechanism of both membranes.

Membranes molecular dynamics study.

To understand the water diffusion within the membrane, we studied the plain PA and the CNF-PA by using classical molecular dynamics simulations. Since molecular dynamics in practice has a limit on the number of atoms simulated, we focused on the region where CNF and PA coexisted. This was presumably the central part of the membrane, even though the plain PA was present in the surface and in contrast CNF was present at the bottom. These simulations were carried out to understand the water diffusion in the bulk of the membrane thus ions, which are mainly rejected by the membrane surface, were excluded from these models.

The two membrane models shown in Figure 3a and 3e were hydrated as described in a previous publication.[50] A video comparing the hydration process of both CNF-PA and PA membranes is shown in Supporting Information (Video S1).
The pore structure is a critical parameter that influences water permeation performance. Thus, we used a void sampling method[51] to characterize the pore size distribution before and after hydration, and the results are shown in Figure 2. A simplified description of the method is the following: first, the spatial structure of the membrane is calculated using the van der Waals radii of the polyamide atoms, then spheres of increasing radius size are probed within the cavities. Finally, the histogram of the radii of the largest spheres that can be fitted inside the pores is calculated. In the dry state, the PA model (Figure 2a) showed a narrower distribution than the CNF-PA model (Figure 2b). After hydration, while the hydrated PA membrane developed a bimodal pore distribution (Figure 2c), the CNF-PA model decreased its average pore size (Figure 2d). The bimodal pore distribution suggests the formation of pockets that might allow high permeation rate of water clusters and ions, as we discussed before.[51] The reduction of pore size of the CNF-PA membrane upon hydration is a consequence of the higher hydrophilicity, because the water is better distributed within the PA matrix. This mixing is the result of small movements of the matrix. On the other hand. the formation of larger pores in the plain PA membrane does
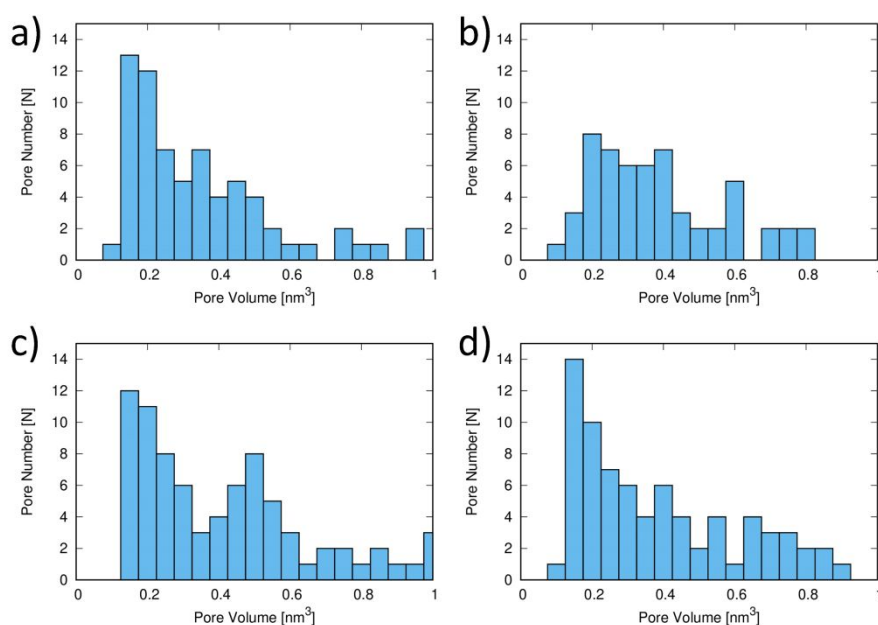
Figure 2. Pore size analysis of the a) dry plain PA sample, b) dry CNF-PA membrane, the respective c) hydrated plain PA, and d) hydrated CNF-PA.

require larger displacements of the bulk matrix to accommodate large pockets of water.

The behaviour upon hydration of the CNF-PA membrane was similar to that shown by the CNT-PA membrane. This is probably because the stiff CNF provides mechanical nanoreinforcement to the membrane, limiting the polymer mobility and avoiding

matrix. The water diffusion coefficient maps of the PA and CNF-PA membranes are shown in Figure 3c and 3g, respectively. Water mobility is dependent on the mobilities of components and hydration degree of the membranes. As expected, the CNF membrane (Figure 3g) showed a diffusion coefficient of 0.37×10^{-5} cm^2/s, which is 40 % higher than the diffusion
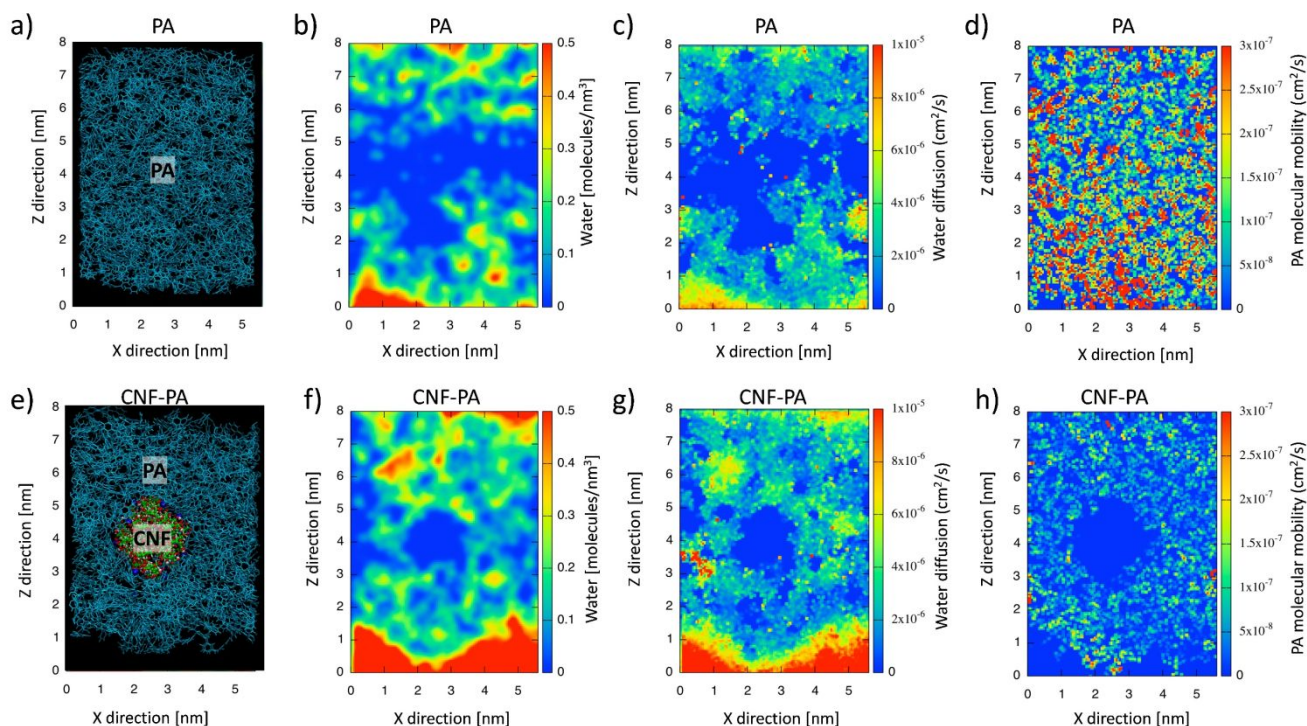
Figure 3. a) PA structure model, b) water density, c) water diffusion coefficient, and d) polymer mobility maps of the aromatic plain polyamide (PA) membrane, e) PA-CNF structure model, f) water density, g) water diffusion coefficient, and h) polymer mobility (only PA part) maps of the CNF-PA membrane.

the deformation of the PA matrix upon hydration. After the membranes shown in Figure 3a and 3e were hydrated, we mapped the PA water diffusion, water content, and polymer mobility of the membranes to study the water diffusion mechanism, and compared the results with those of the CNF-PA membrane. Detailed explanation of the procedure to obtain the maps is shown in Figure S7. The water content of both the PA and CNF-PA membranes were assessed from Figures 3b and 3f, respectively. The sodium ions present as counterions of the carboxy groups in CNF increased dramatically the hydrophilicity of the membrane, resulting in a water content of 16.2 wt% (Figure 3f), which was higher than that of the plain PA (Figure 3b) with 11.6 wt%. The higher water content of the CNF-PA membrane is due to the hydrophilic nature of the sodium carboxylate groups. Indeed, TEMPO oxidized CNFs prepared by TEMPO mediated oxidation contains abundant sodium carboxylate groups in the surface.[30] When the CNF has protonated carboxy groups in place of sodium carboxylate groups, the CNF might become less hydrophilic because of the low pKa (~3.5) of carboxyl groups.

The PA membrane showed some areas with non-hydrated pockets, which suggested lack of hydration ability of the PA

coefficient, 0.21×10^{-5} cm^2/s, of the plain PA membrane (Figure 3b). The increment in the water diffusion rate is ascribed in part to long-distance interaction with the anionic sodium carboxylate groups on the CNF surface, because the PA components located in the proximity of the CNF fiber did not hydrate during the simulation, most likely owing to their strong CNF-PA interactions. However, this interaction between CNF and PA components is also necessary to avoid failure at the CNF-PA interface due to stress induced by the small changes in the membrane pressure operation. The reduction of pore size upon hydration is a consequence of the higher hydrophilicity, because the water is better distributed/mixed with the matrix. This mixing is the result of small movements of the matrix. On the other hand. the formation of larger pores in the plain PA membrane does require larger displacements of the bulk matrix to accommodate large pockets of water. The calculated coefficient of water diffusion (0.21×10^{-5} cm^2/s) is similar or in the same order of magnitude with previously reported values found by MDs such as Kotleyanski et al.[52] (0.20×10^{-5} cm^2/s), Hughes and Gale[53] (0.21×10^{-5} cm^2/s), Kolev and Freger[54] (0.5×10^{-5} cm^2/s) and and Xiang et al.[55] (0.12×10^{-5} cm^2/s). The difference between different values reported are due to the use

of different force fields and water models during the simulations.

We studied the effect of the PA and CNF-PA molecular mobility obtained by mapping the PA mobility (Figures 3d and 3h, respectively). The molecular stiffening effect of the CNF is clear when we compared the average mobility of the PA of 2.76×10^{-7} cm2/s to the average value of the CNF containing membranes, which was 1.59×10^{-7} cm^2/s, a considerably lower value. It is clear the CNF conferred stiffness to the PA matrix although the sodium carboxylate groups should still contribute to improve the hydrophilicity of the PA-CNF membrane. The reason why the salt rejection rate was very similar might be related to the similar composition of the top layers in both membranes, where most of the salt rejection rate in nanocomposite membranes takes place.[56] Conventional plain PA active membranes usually follow a tradeoff between salt-rejection and permeability: higher salt rejection means lower permeability. The reason is usually because the structure of the active layer is homogeneous, and a small pore size in the top-layer means that also the bulk of the membrane will have a small pore size, resulting in a slow water diffusion across the membrane. Nanocomposite active layers have attracted attention in the last years because they can break this tradeoff, and one of the proposed reasons is because the composition of the active layer is not homogenous. We believe the active layer of our membrane combines a dense top-layer with good salt rejection with a high-flux region reinforced with CNFs. Recently, cellulose nanomaterials have been used as active layer additives in polyamide membranes. Bai *et al.*,[42,43] synthesized piperazine-based polyamide membranes containing CNCs. The flux was improved and even though the sodium chloride rejection was relatively low, up to 98.7% and 98.8% rejection rate for Na_2SO_4 and MgSO4 was achieved. They concluded that CNCs can improve the flux of these nanofiltration membranes without compromising the salt rejection. Similar results were obtained by Huang et al.[44] in membranes made also with piperazine monomer. In the case of aromatic polyamides, Asempour *et al*.[45] found that CNCs loaded aromatic polyamide membranes improved their flux while a slight reduction in salt rejection occurred as the fraction of CNCs in the composite membrane increased. Interestingly, they added the CNCs to the organic phase, thus they might be located on or near the surface of the membrane and might be one reason why the salt rejection decreased. On the other hand, Liu *et al.*[34] prepared nanocomposite membrane using aromatic polyamide and tempo-oxidized CNFs. They found improvement in both flux and chlorine resistance, while the salt rejection reached values as high as 96.2 % when using 2000 ppm sodium chloride solution. In general, previous results and this work show that nanocomposite aromatic polyamide membranes containing CNFs have great potential in the synthesis of desalination membranes.

Membranes fouling study.

Besides the high-water permeation rate, other advantages desired on RO membranes are antifouling and chlorine resistance performance. We studied the fouling of bovine serum albumin (BSA) on the CNF-PA membrane and compared it with the plain PA membrane (Figure 4). Even though alginates are more common foulants in desalination membranes, BSA is often used as a model foulant because its mechanisms of adsorption are well known. The most important and pragmatic parameter to judge the membrane fouling is its relative water permeability, shown in Figure 4a. The CNF-PA membrane slightly decreased its water permeation rate (~10% from the initial value) after 140 h. In contrast, the plain PA membrane quickly reduced the water permeation rate to ~40 % from its initial value after 24 h, and then the permeation rate was stabilized afterwards. In the case of PA, this behavior consisted of the quick formation of a thin layer of foulant at on the PA membrane surface that decreased the permeation rate.The relative amount of foulant deposited on the membrane surface was assessed by fluorescence measurements (Figure 4b) obtained from the images (figure 4c). By comparing the fluorescence measurements with the relative water permeability in Figure 4a, it seems that even though more amounts of foulant were deposited only on the first layer, which might have significant impact on the water permeability. There was also noticeable foulant deposits at the gap between the spacer located in the surface of the membrane and the membrane surface (Figure 4c), which was most likely due to the combined effect of restricted water flow and the hydrophobic effect of the spacer.[57]

In the case of the CNF-PA membrane, the deposition of foulant was considerably decreased, and after 144 h most of the green signals were observed at the spacer. In the case of the PA membrane, the integrated fluorescence signal from the central area (Figure 4b) shows a constant increment over time. These results showed that both membranes had fouling phenomena, as shown from the fluorescence images. However, the water permeability of the PA membrane had higher foulant deposition than the CNF-PA membrane, indicating different membrane-foulant interaction between the two membranes.

Then, we carried out molecular dynamics simulations to understand the process of foulant deposition behavior at the molecular level in the membranes. The trajectory of the fouling simulations is shown in Supporting Information video S2. During the simulation, we equilibrated a BSA molecule on the surface of a model membrane, which was then applied to water flow. , in the long run, a slow ion-exchange between the remaining free carboxylic groups of the CNF and the Na$^+$ is possible, thus we included the two cases in the simulation videos. The distance from the center of mass to the membrane surface and its velocity are shown in Figure 4e. The velocity of BSA movement during the simulation is shown in Figure 4e. The attractive forces between the BSA molecule and the PA membrane surface were high, resulting in the close interaction between the two components. The continuous interaction between the two components also contributed to a decrease in the mobility of BSA molecule. In the case of the CNF-PA model, the BSA molecule maintained a longer distance from the membrane surface, resulting in a higher terminal velocity of the BSA molecule. The Na$^+$ ions decrease the negative charge of the

CNF and decrease the repulsion to the BSA. The supp. inf. video shows that substitution of the carboxyl groups with sodium carboxylate groups decrease the effectiveness of the CNF-PA membrane against fouling, but is still better than the plain PA. These simulation also suggest that repulsion of the BSA is mainly due to long electrostatic charges in the simulation, although in the experimental case, surface roughness and decreased

We tested the CNF-PA and the reference PA membranes to 20 ppm active chlorine test and evaluated the water permeability and salt rejection rate (Figure 5). During the first 100 h, both membranes remained constant values, however, after this induction time, the plain PA membrane quickly decreased its salt rejection rate and significantly increased its water permeation rate, because of the rapid degradation of the PA
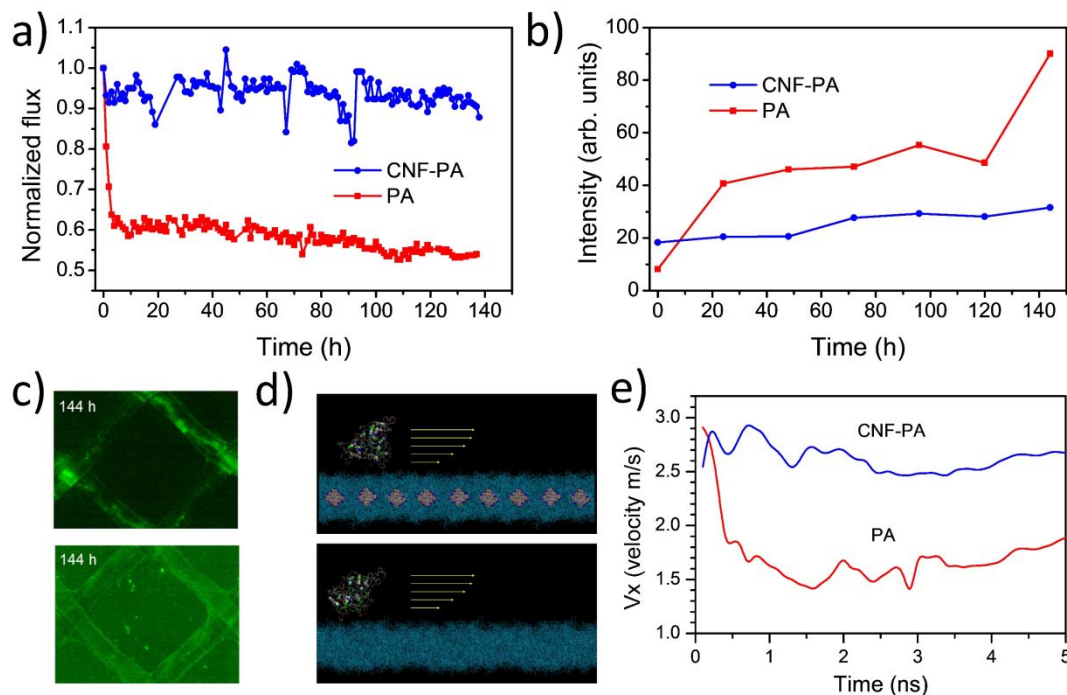
Figure 4. Fouling studies on the CNF-PA and PA membranes. a) Normalized flux data, b) semiquantitative analysis of the fluorescence of the membranes surfaces during the fouling tests, c) fluorescence microscopy images of the membrane surfaces after 144h of fouling: top CNF-PA and bottom plain PA. d) Molecular dynamics models of the fouling simulations. e) Instantaneous speed calculation of the BSA molecule during a desorption process simulated by molecular dynamics.

molecular mobility of the membrane might also contribute to improve the antifouling properties of the CNF-PA membrane.

The BSA molecule had a negative charge in water at near-neutral conditions because its isoelectric point is 4.7. The model CNF-PA membrane contained 66% of carboxy groups, and 33% of them had sodium carboxylate structures (see Figure S2). Since the CNF used in this study also had negatively charged sites, it is possible that long range electrostatic repulsion drive away the anionic BSA molecule from the surface for the CNF-PA membranes. In the practice, the antifouling performance might also be improved, because the CNF-PA membrane had a smoother surface, and it has been reported that smooth surface membranes usually have better antifouling performance.[58]

Chlorine resistance

membrane by chlorine.

The CNF-PA membrane also started to degrade at the same time, but its degradation rate was lower. In this stage, the water permeation rate decreased because the PA matrix in the CNF-PA membrane suffered chlorination and became more hydrophobic. This phenomenon has been seen in other plain PA membranes, and this is the first step of degradation before rearrangement of the PA molecules in the membrane.[59,60] We use the 97.5% salt rejection mark to compare the potential lifetime under these conditions. The plot shows that the CNF-PA membrane took twice the time compared to the plain PA membrane to reach this critical point.

The chemical stability of the membranes was confirmed by studying the bulk powders of PA and PA-CNF by several characterization techniques (Figure S8). In the bulk, the chlorination of PA was accompanied with yellowing because of the formation of imide bonds as well as a degradation of the powder form. We exposed the PA and CNF-PA powders to 4800 ppm/h chlorination under stirring. After the chlorination, the materials suspended in water were left standing (Figure S8a). The lower yellowing and the apparently lower amount of

suspended materials revealed a protective effect of CNF in the membrane against chlorine.

The chlorinated powder materials were washed with water and then methanol and dried for further analyses. The TGA patterns are shown in Figure S8b. TEMPO-CNF had a considerably lower degradation temperature than aromatic PA; therefore, the CNF-PA composite had lower thermal stability than PA. However, the chlorination treatment resulted in an improvement of thermal stability for the CNF-PA, whereas the PA showed the opposite result.
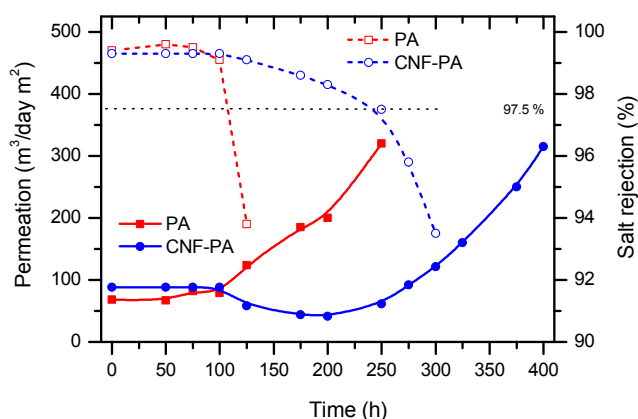
Figure 5. Evolution of the water permeation rate (left) and salt rejection rate (right) during continuous chlorine exposure at 20 ppm for the CNF-PA membrane and the laboratory-made plain PA membrane.

Figure S8c shows the FTIR spectra from 4000 cm^{-1} to 400 cm^{-1} and Figure S8d shows the area corresponding to the bond stretching bands range magnified. Chlorine degradation of the membranes was accompanied by hydrolysis of PA, the degree of which can usually be determined from the ratio of the carboxy to amide bond absorption intensities (A_{1606}/A_{1656}). Surprisingly, after the chlorine treatment, the A_{1606}/A_{1656} absorption ratio of the CNF-PA membrane was as low as 1.25, a value slightly higher than that of the plain PA. This suggest than the role of CNF to protect from chlorine degradation does not prevent the hydrolysis of the membrane.

This result indicates that the CNF had a high resistance to the chlorine-degradation of PA molecules; therefore, the chlorine resistance of the CNF-PA might be imparted from the structural point of view as follows. The chlorine resistant of the CNF-PA membrane prevented pinhole formation, reducing the diffusion of chlorine and keeping the mesostructure of the membrane intact. This hypothesis was also supported from the XPS spectra of the membranes before and after chlorination (Figure S9a and S9b). The amount of covalent C-Cl observed in Figure S9b was similar in both membranes, which is not surprising because both membranes had PA-rich structure on the surface. Thus, it is likely that the CNF reinforcement is enough to protect the mechanical properties of the PA membrane rather than provide chemical antichlorination activity, but it is possible that CNF also decreased the reactivity of chlorine molecules with the PA membrane, by stiffening the PA molecular structure.

Conclusions

Tempo-oxidized CNF was used to improve the water permeation rate, antifouling and chlorine resistance properties of the aromatic PA membranes. The synthesis was carried out by dispersing the CNF in the aqueous phase and performing the interfacial synthesis as usual. The presence of sodium carboxylate groups of CNF within the CNF-PA membrane improved the water diffusion rate, while the chlorine-resistance of CNF contributed to improvement of the stability of the membrane against chlorination. The slight decrease in surface roughness and the presence of negatively charged TEMPO-CNF may have also improved the antifouling against negatively charged BSA molecules. These results make CNF-PA membranes a material with great potential to be used in reverse osmosis desalination membranes for seawater.

Experimental

Reverse osmosis membranes preparation

TEMPO-oxidized CNF gel (Rheocrysta 2.0 wt% in water) was kindly provided by the manufacturer. All other reagents were of analytical grade. Except otherwise indicated, nanocomposite CNF-PA membranes were prepared by interfacial polymerization of *m*-phenylendiamine (MPD) and trimesoyl chloride (TMC) using the following method: First, the aqueous phase was prepared by dissolving the following reagents in deionized water until the indicated concentration was reached: CNF (0.2 wt%), MPD (2.5 wt%), camphorsulfonic acid (5.0 wt%), triethyl amine (2.5 wt%), sodium dodecyl sulfate (0.15 wt%) and isopropyl alcohol (6.0 wt%). This aqueous reaction mixture was coated on a non-functionalized polysulfone support membrane (X-ray photoelectron spectroscopy of the plain membrane is shown in Figure S10) and left to impregnate for 5 minutes under the fume hood. After removing the excess reaction mixture, a freshly prepared solution of TMC on IP solvent 1016 (0.18 wt%) was spread onto the membrane and allowed to polymerize for 60 seconds. The membrane was then transferred to an oven where it was dried for 3 minutes at 120 ºC. The membrane was finally washed with water for several hours and kept wet until the water permeation measurements. X-ray photoelectron spectroscopy (XPS) analysis showed that washing could remove any residual sulfur; thus the membrane was free of camphorsulfonic acid or sodium dodecyl sulfate. Plain aromatic PA membranes for comparison were prepared similarly but using a relatively simple recipe of 2.0 wt % of *m*-metaphenylendiamine (MPD) in water and 0.1 % of trimesoylchloride (TMC) as the aqueous phase.

Fouling studies.

We carried out BSA fouling testing on the membranes by monitoring the water permeation rate and in situ fouling deposition using fluorescence microscopy as recently reported by our group.[26] Briefly, membranes were compacted by running 2 h under 5.5 MPa using DI water. After measuring the water permeability and salt rejection rate using a 3.5 wt% saline solution at 5.5 MPa, the membrane was fed with a 100 ppm

solution of fluorescein thiocyanate labeled BSA dissolved in 10 mmol sodium chloride solution in a pH 10 buffer. A laboratory-made acrylic resin cross-flow cell was used to observe the membrane fouling process by fluorescence microscopy in real-time during 144 h using a Nikon SMZ18 fluorescence microscope equipped with a CMOS digital camera (Model MC500, Ostec, Guanzhou, China). Exposure time was kept at 196 ms, and blue excitation light (490 nm) was used with a Nikon P2-EFLC green filter.

Molecular dynamics simulations.

Molecular dynamics simulations were used to study the hydration and water permeation of the different membrane models. The primary CNF structures were built using the nanocellulose builder program,[61] and modified to include the carboxy groups on the surface to match the composition reported by Isogai et al.[32] as shown in Figure S10. Using this CNF model, we prepared a model CNF-PA composite membrane as shown in Figure S7a and compared it with the fully aromatic PA membrane used as a reference. The method used to construct the PA membrane and the CNF-PA membrane models is similar to that reported in our previous study of carbon nanotubes-composite membranes.[29,50]

The composite membrane model was built by running a molecular dynamics simulation, allowing the adsorption of MPD molecules on the CNF surface, followed by the *in silico* polymerization process of these seeds. The formation of topological defects, such as rings and hydrolysis of unreacted acyl groups, was considered in the polymerization process. The process targets not only the density of PA but also the content of carboxy groups and the crosslinking degree.[50] After the structure was built, an isothermal–isobaric (NPT) relaxation was achieved by maintaining the total pressure at 1 atm, while the structure was relaxed during 200 ps using 0.5 fs steps. The charge equilibration method (QEq) was used to calculate the distribution of charges in the large system.[62] During the simulations, the SPC/E model[63] was adopted for the water molecules. For the PA atoms we used the General Amber Force Field (GAFF)[64] while for the CNF we used the CHARMM force field to for the interaction of the molecules which have shown before to reproduce well values such as hydration, diffusion, and density in these chemical structures.[50,65,66]

The interactions between molecules were considered, based on Lennard-Jones (LJ) and Coulomb interactions with particle-particle mesh solver (P3M).[67] All MD simulations were performed with setting the time step of 1.0 fs, and the trajectory data were saved at 10,000-step intervals for analysis using the LAMMPS code.[68] To calculate the maps of charge density, diffusion, and molecular mobility, the mesh was set to 0.2 Å. The distance criteria for hydrogen bonds was set to ≤4.0 Å. All calculations were performed inside a unit cell under periodic conditions. The pore size of the membrane was probed using the algorithm described by Bhattacharya and Gubbins.[51] The volume of the atoms was estimated as spheres with their van der Waals radii, while the CNF was excluded from this analysis. Image rendering was done using visual molecular dynamics software.[69]

Characterization.

Fourier transform infrared spectroscopy (FTIR) spectra of the PA and PA-CNF membranes and powders were obtained by attenuated total reflectance mode, whereas the FTIR of the CNFs was obtained by transmission mode using a very thin CNF cast film. X-ray photoelectron spectroscopy (XPS) was carried on a PHI Quantera II (Ulvac-Phi, Japan) with monochromatic Al Kα source. The spot size used was 100 μm in diameter and all spectra were charge-normalized using the peak at the lowest binding energy peak (284.5 eV) in C 1s core-level spectrum as a reference. The membrane surfaces were observed by a scanning electron microscope (SEM) using a SU8000 ultrahigh performance SEM (Hitachi, Japan) and a FE-SEM 7000F (JEOL, Japan). Atomic force microscopy (AFM) images were obtained in tapping mode. The CNF dispersion was diluted and dried on a silicon wafer. Free standing PA and CNF-PA membranes were obtained by dissolving the polysulfones support membrane and washing the membranes three times with dimethylformamide and methanol. Thermogravimetric analysis (TGA) was carried out for the membrances in air at a heating rate of 5 °C/min. High resolution transmission electron microscopy (HR-TEM) and scanning transmission electron microscopy (STEM) study was carried out using JEM-2100F (JEOL, Japan) equipped with aberration correctors (CETCOR & CESCOR, CEOS, Germany) operated at 80 kV.

Authors contribution

K.I, J.M., and S.S. synthesis and measured desalination and permeation, desalination and chlorine resistance. A.M.G. and C.A. carried out XPS, Raman, FTIR spectroscopy, and sample preparation. Y.T. Carried out the fouling study, A.Y. and S.T. carried out molecular dynamics study, K.F and T.H. Carried out TEM and STEM observations. R.C.S., K.T., T.N, and A.I. analyzed and discussed the experimental results, R.C.S. and M.E. coordinated the project and wrote the first draft. All authors read and discussed the manuscript.

Conflicts of interest

There are no conflicts to declare.

Acknowledgements

Notes and references

1   K. P. Lee, T. C. Arnot and D. Mattia, Journal of Membrane Science, 2011, 370, 1-22.

2   S. Manju and N. Sagar, Renewable & Sustainable Energy Reviews, 2017, 73, 594-609.

3   E. Hanak and J. R. Lund, Climatic Change, 2012, 111, 17-44.

4   N. V. Paranychianakis, M. Salgot, S. A. Snyder and A. N. Angelakis, Critical Reviews in Environmental Science and Technology, 2015, 45, 1409-1468.

5   S. Loeb and S. Sourirajan, in Saline Water Conversion—II, AMERICAN CHEMICAL SOCIETY, 1963, vol. 38, ch. 9, pp. 117-132.

6   J. E. Cadotte, Reverse Osmosis Membranes, US Patent, US3926798A, 1975.

7   D. J. Miller, D. R. Dreyer, C. W. Bielawski, D. R. Paul and B. D. Freeman, Angewandte Chemie-International Edition, 2017, 56, 4662-4711.

8   X. D. You, T. Y. Ma, Y. L. Su, H. Wu, M. Y. Wu, H. W. Cai, G. M. Sun and Z. Y. Jiang, Journal of Membrane Science, 2017, 540, 454-463.

9   J. T. Duan, E. Litwiller and I. Pinnau, Journal of Membrane Science, 2015, 473, 157-164.

10 M. L. Lind, A. K. Ghosh, A. Jawor, X. F. Huang, W. Hou, Y. Yang and E. M. V. Hoek, Langmuir, 2009, 25, 10139-10145.

11 B. H. Jeong, E. M. V. Hoek, Y. S. Yan, A. Subramani, X. F. Huang, G. Hurwitz, A. K. Ghosh and A. Jawor, Journal of Membrane Science, 2007, 294, 1-7.

12 W. F. Chan, H. Y. Chen, A. Surapathi, M. G. Taylor, X. H. Hao, E. Marand and J. K. Johnson, Acs Nano, 2013, 7, 5308-5319.

13 M. Amini, M. Jahanshahi and A. Rahimpour, Journal of Membrane Science, 2013, 435, 233-241.

14 L. Zhang, G. Z. Shi, S. Qiu, L. H. Cheng and H. L. Chen, Desalination and Water Treatment, 2011, 34, 19-24.

15 J. N. Shen, C. C. Yu, H. M. Ruan, C. J. Gao and B. Van der Bruggen, Journal of Membrane Science, 2013, 442, 18-26.

16 J. Xu, Z. Wang, L. L. Yu, J. X. Wang and S. C. Wang, Journal of Membrane Science, 2013, 435, 80-91.

17 H. Y. Zhao, S. Qiu, L. G. Wu, L. Zhang, H. L. Chen and C. J. Gao, Journal of Membrane Science, 2014, 450, 249-256.

18 H. J. Kim, M. Y. Lim, K. H. Jung, D. G. Kim and J. C. Lee, Journal of Materials Chemistry A, 2015, 3, 6798-6809.

19 H. J. Kim, K. Choi, Y. Baek, D. G. Kim, J. Shim, J. Yoon and J. C. Lee, Acs Applied Materials & Interfaces, 2014, 6, 2819-2829.

20 S. Inukai, R. Cruz-Silva, J. Ortiz-Medina, A. Morelos-Gomez, K. Takeuchi, T. Hayashi, A. Tanioka, T. Araki, S. Tejima, T. Noguchi, M. Terrones and M. Endo, Scientific Reports, 2015, 5, 10.

21 A. Tiraferri, C. D. Vecitis and M. Elimelech, Acs Applied Materials & Interfaces, 2011, 3, 2869-2877.

22 V. Vatanpour, M. Safarpour, A. Khataee, H. Zarrabi, M. E. Yekavalangi and M. Kavian, Separation and Purification Technology, 2017, 184, 135-143.

23 J. Park, W. Choi, S. H. Kim, B. H. Chun, J. Bang and K. B. Lee, Desalination and Water Treatment, 2010, 15, 198-204.

24 R. Cruz-Silva, Y. Takizawa, A. Nakaruk, M. Katouda, A. Yamanaka, J. Ortiz-Medina, A. Morelos-Gomez, S. Tejima, M. Obata, K. Takeuchi, T. Noguchi, T. Hayashi, M. Terrones and M. Endo, Environmental Science & Technology, 2019, 53, 6255-6263.

25 Y. Takizawa, S. Inukai, T. Araki, R. Cruz-Silva, J. Ortiz-Medina, A. Morelos-Gomez, S. Tejima, A. Yamanaka, M. Obata, A. Nakaruk, K. Takeuchi, T. Hayashi, M. Terrones and M. Endo, Acs Omega, 2018, 3, 6047-6055.

26 Y. Takizawa, S. Inukai, T. Araki, R. Cruz-Silva, N. Uemura, A. Morelos-Gomez, J. Ortiz-Medina, S. Tejima, K. Takeuchi, T. Kawaguchi, T. Noguchi, T. Hayashi, M. Terrones and M. Endo, Acs Applied Materials & Interfaces, 2017, 9, 32192-32201.

27 N. Zarrabi, M. E. Yekavalangi, V. Vatanpour, A. Shockravi and M. Safarpour, Desalination, 2016, 394, 83-90.

28 J. Ortiz-Medina, S. Inukai, T. Araki, A. Morelos-Gomez, R. Cruz-Silva, K. Takeuchi, T. Noguchi, T. Kawaguchi, M. Terrones and M. Endo, Scientific Reports, 2018, 8.

29 T. Araki, R. Cruz-Silva, S. Tejima, J. Ortiz-Medina, A. Morelos-Gomez, K. Takeuchi, T. Hayashi, M. Terrones and M. Endo, Physical Review Applied, 2018, 9.

30 A. Isogai, T. Saito and H. Fukuzumi, Nanoscale, 2011, 3, 71-85.

31 N. Lin and A. Dufresne, European Polymer Journal, 2014, 59, 302-325.

32 T. Saito, S. Kimura, Y. Nishiyama and A. Isogai, Biomacromolecules, 2007, 8, 2485-2491.

33 H. Kargarzadeh, M. Mariano, J. Huang, N. Lin, I. Ahmad, A. Dufresne and S. Thomas, Polymer, 2017, 132, 368-393.

34 S. S. Liu, Z. X. Low, H. M. Hegab, Z. L. Xie, R. W. Ou, G. Yang, G. P. Simon, X. W. Zhang, L. Zhang and H. T. Wang, Journal of Membrane Science, 2019, 592.

35 K. Liu, Abstracts of Papers of the American Chemical Society, 2017, 254.

36 C. H. Park, S. Jeon, S. H. Park, M. G. Shin, M. S. Park, S. Y. Lee and J. H. Lee, Journal of Materials Chemistry A, 2019, 7, 3992-4001.

37 E. D. Smith, K. D. Hendren, J. V. Haag, E. J. Foster and S. M. Martin, Nanomaterials, 2019, 9.

38 M. S. Reid, J. Erlandsson and L. Wagberg, Acs Macro Letters, 2019, 8, 1334-1340.

39 E. Smith and S. Martin, Abstracts of Papers of the American Chemical Society, 2017, 254.

40 J. J. Wang, H. C. Yang, M. B. Wu, X. Zhang and Z. K. Xu, Journal of Materials Chemistry A, 2017, 5.

41 J. L. Lv, G. Q. Zhang, H. M. Zhang and F. L. Yang, Carbohydrate Polymers, 2017, 174, 190-199.

42 L. M. Bai, Y. T. Liu, A. Ding, N. Q. Ren, G. B. Li and H. Liang, Chemical Engineering Journal, 2019, 358, 1519-1528.

43 L. M. Bai, Y. T. Liu, N. Bossa, A. Ding, N. Q. Ren, G. B. Li, H. Liang and M. R. Wiesner, Environmental Science & Technology, 2018, 52, 11178-11187.

44 S. Huang, M. B. Wu, C. Y. Zhu, M. Q. Ma, J. Yang, J. Wu and Z. K. Xu, Acs Sustainable Chemistry & Engineering, 2019, 7, 12315-12322.

45 F. Asempour, D. Emadzadeh, T. Matsuura and B. Kruczek, Desalination, 2018, 439, 179-187.

46 P. Cruz-Tato, E. O. Ortiz-Quiles, K. Vega-Figueroa, L. Santiago-Martoral, M. Flynn, L. M. Diaz-Vazquez and E. Nicolau, Environmental Science & Technology, 2017, 51, 4585-4595.

47 D. Trache, M. H. Hussin, M. K. M. Haafiz and V. K. Thakur, Nanoscale, 2017, 9, 1763-1786.

48 T. Saito, Y. Nishiyama, J. L. Putaux, M. Vignon and A. Isogai, Biomacromolecules, 2006, 7, 1687-1691.

49 F. Pacheco, R. Sougrat, M. Reinhard, J. O. Leckie and I. Pinnau, Journal of Membrane Science, 2016, 501, 33-44.

50 T. Araki, R. Cruz-Silva, S. Tejima, K. Takeuchi, T. Hayashi, S. Inukai, T. Noguchi, A. Tanioka, T. Kawaguchi, M. Terrones and M. Endo, Acs Applied Materials & Interfaces, 2015, 7, 24566-24575.

51 S. Bhattacharya and K. E. Gubbins, Langmuir, 2006, 22, 7726-7731.

52 T. Araki, R. Cruz-Silva, S. Tejima, K. Takeuchi, T. Hayashi, S. Inukai, T. Noguchi, A. Tanioka, T. Kawaguchi, M. Terrones and M. Endo, Acs Applied Materials & Interfaces, 2015, 7, 24566-24575.

53 M.J. Kotelyanskii, N.J. Wagner, M.E. Paulaitis, Comput. Theor. Polym. Sci., 1999, 9, 301-306.

54 Z.E. Hughes, J.D. Gale, J. Mater. Chem. 2010,20, 7788-7799.

55 V. Kolev, V. Freger, J Phys. Chem. B, 2015, 119, 14168-14179.

56 Y. Xiang, Y. Liu, B. Mi, Y. Lengm Langmuir, 2013,29, 11600-11608.

57 M. Fathizadeh, A. Aroujalian and A. Raisi, Journal of Membrane Science, 2011, 375, 88-95.

58 H. Kitano, K. Takeuchi, J. Ortiz-Medina, R. Cruz-Silva, A. Morelos-Gomez, M. Fujii, M. Obata, A. Yamanaka, S. Tejima, M. Fujishige, N. Akuzawa, A. Yamaguchi and M. Endo, Acs Omega, 2019, 4, 15496-15503.

59 M. Elimelech, X. H. Zhu, A. E. Childress and S. K. Hong, Journal of Membrane Science, 1997, 127, 101-109.

60 G. D. Kang, C. J. Gao, W. D. Chen, X. M. Jie, Y. M. Cao and Q. Yuan, Journal of Membrane Science, 2007, 300, 165-171.

61 J. Ortiz-Medina, Z. P. Wang, R. Cruz-Silva, A. Morelos-Gomez, F. Wang, X. D. Yao, M. Terrones and M. Endo, Advanced Materials, 2019, 31.

62 T. C. F. Gomes and M. S. Skaf, Journal of Computational Chemistry, 2012, 33, 1338-1346.

63 A. K. Rappe and W. A. Goddard, Journal of Physical Chemistry, 1991, 95, 3358-3363.

64 H. J. C. Berendsen, J. R. Grigera and T. P. Straatsma, The Journal of Physical Chemistry, 1987, 91, 6269-6271.

65 W. D. Cornell, P. Cieplak, C. I. Bayly, I. R. Gould, K. M. Merz, D. M. Ferguson, D. C. Spellmeyer, T. Fox, J. W. Caldwell and P. A. Kollman, Journal of the American Chemical Society, 1995, 117, 5179-5197.

66 Y. Luo, E. Harder, R. S. Faibish and B. Roux, Journal of Membrane Science, 2011, 384, 1-9.

67 E. Harder, D. E. Walters, Y. D. Bodnar, R. S. Faibish and B. Roux, Journal of Physical Chemistry B, 2009, 113, 10177-10182.

68 E. L. Pollock and J. Glosli, Computer Physics Communications, 1996, 95, 93-110.

69 S. Plimpton, Journal of Computational Physics, 1995, 117, 1-19.

70 W. Humphrey, A. Dalke and K. Schulten, Journal of Molecular Graphics & Modelling, 1996, 14, 33-38.

203x101mm (600 x 600 DPI)